Calculation of the emission power distribution of microstructured OLEDs using the reciprocity theorem

Shuyu Zhang[1)], Emiliano R. Martins[1)], Adel G. Diyaf[2,3)], John I.B. Wilson[3)], Graham A. Turnbull[1)]*, Ifor D.W. Samuel[1)]*

1) *Organic Semiconductor Centre, SUPA, School of Physics and Astronomy, University of St. Andrews, North Haugh, St. Andrews, Fife KY16 9SS, UK*

2) *Faculty of Science, Physics Department, Tripoli University, P.o. Box 13281, Tripoli, Libya.*

3) *School of Engineering and Physical Sciences, Heriot-Watt University, Edinburgh, EH14 4AS, UK*

*Corresponding authors

E-mail addresses: gat@st-andrews.ac.uk; idws@st-andrews.ac.uk

Abstract

Integrating photonic microstructures into organic light-emitting diodes (OLEDs) has been a widely used strategy to improve their light out-coupling efficiency. However, there is still a need for optical modelling methods which quantitatively characterise the spatial emission pattern of microstructured OLEDs. In this paper, we demonstrate such rigorous calculation using the reciprocity theorem. The calculation of the emission intensity at each direction in the far field can be simplified into only two simple calculations of an incident plane wave propagating from the far field into a single cell of the periodic structure. The emission from microstructured OLED devices with three different grating periods was calculated as a test of the approach, and the calculated results were in good agreement with experiment. This optical modelling method is a useful calculation tool to investigate and control the spatial emission pattern of microstructured OLEDs.

Key words:

Organic light-emitting diode; Photonic microstructures; Optical modelling; Reciprocity theorem; Spatial emission pattern

1. Introduction

OLEDs which contain lateral photonic microstructures are of interest for a number of different applications. Most commonly they have been used to improve the OLED external quantum efficiency, by out-coupling the light trapped in substrate modes, waveguide modes and surface plasmon polaritons [1-11]. To use such devices in displays or lighting applications, such microstructured OLEDs must be designed to provide good angular colour stability. Photonic microstructures have also been studied for other applications, such as developing OLEDs with directional emission [12, 13], where a strong contrast of emission intensity across different viewing angles is required.

For a typical microstructured OLED, the overall far field emission pattern is composed of the out-coupled emission of the trapped modes superimposed on a spatially broad background emission. The broad background is due to the light which was directly emitted from the OLED with wavevectors within the light escape cone and thus not affected by the photonic microstructures. Currently the most common method to model the spatial emission pattern of a microstructured OLED is simply to analyse the photonic dispersion of a grating by the Bragg condition [14-17]. This calculates the out-coupling elevation and azimuthal angles of trapped modes, but does not provide information about the relative power distribution of the far field emission. Alternative optical modelling methods which calculate quantitatively the far field spatial power distribution from microstructured OLEDs are therefore needed.

A full quantitative analysis of the far field emission pattern requires a rigorous solution to Maxwell's equations. The radiating molecules within the OLED can be described as classical forced electric dipole

oscillators distributed in the active layer [18, 19]. Such dipoles can have different orientations and emission frequencies and incoherently contribute to the far field emission pattern. The electromagnetic (EM) waves of the dipoles generated inside the OLED structure are affected by the multiple reflections of the OLED cavity, complicating the optical modelling of OLEDs. In practice, a large number of dipoles need to be used to accurately calculate the spatial emission pattern in such a method, which consumes extensive computational resources. Rigorous methods such as finite-difference time-domain (FDTD), finite element method (FEM) and rigorous coupled-wave analysis (RCWA) have been used to investigate the enhancement of the light out-coupling efficiencies of microstructured OLEDs by distributing a large number of dipoles in the active layer and integrating the energy extracted into air [20-25]. Apart from such forward methods, Zhang *et al.* investigated the modes in the microstructured OLEDs in a reverse way by sending an EM plane wave into the OLED at normal incidence and investigating how efficiently it can be coupled into a waveguide [26]. This reported modelling focused on the improvement in light out-coupling efficiencies, however, they did not address the calculation of spatial amplitude of the emission pattern from microstructured OLEDs in the far field, and the need to address such calculations is increasing in the OLED community [1-13].

In this paper, we develop an efficient optical modelling method based on the Lorentz reciprocity theorem [27, 28] to quantitatively characterise the spatial emission pattern of microstructured OLEDs. This theorem has not been applied to calculate the spatial emission pattern of OLEDs before. The key idea of the reciprocity theorem is to convert a light out-coupling problem of an OLED into a light in-coupling problem [29-32]. It significantly simplifies the simulation and provides the information of the spatial emission pattern in a computationally efficient calculation. In **Section 2**, the theory of the Lorentz

reciprocity theorem and the calculation methods used are introduced. The experimental details of device fabrication and testing are described in **Section 3**. A test of the model is presented in **Section 4**. The calculation results are compared with experimental results to verify the accuracy of the modelling.

2. Theory and calculation

The Lorentz reciprocity theorem states that the relationship between a localised oscillating current and the resulting electric field is unchanged if the positions where the current is placed and where the field is measured are swapped [32, 33].

$$\iiint \vec{E}_{J_1} \cdot \vec{J}_2 d^3\vec{r} = \iiint \vec{E}_{J_2} \cdot \vec{J}_1 d^3\vec{r} \quad (1)$$

$\vec{J}$ is the localised time-harmonic current density oscillating at an angular frequency of ω, and $\vec{E}$ is the resulting electric field produced by the current density, with subscripts as defined in **Fig. 1a**. The theorem is valid for absorbing and anisotropic media, but not for nonlinear media. If the current densities are generated by point-like dipole sources, the relationship between the current density and dipole moment is given by

$$\vec{J}_m = -i\omega\vec{p}_m\delta(\vec{r} - \vec{r}_m) \quad (2)$$

where $\vec{p}_m$ is the dipole moment and subscript m = 1 or 2. Then **Eq. 1** can be simplified into **Eq. 3**.

$$\vec{E}_{p_1} \cdot \vec{p}_2 = \vec{E}_{p_2} \cdot \vec{p}_1 \quad (3)$$

Since the radiating molecules of an OLED can be described as an ensemble of classical forced electric dipoles oscillating at their emissive frequencies, according to **Eq. 3**, the electric field $\vec{E}_{p_1}$ of the emission in a specific direction in the far field by a dipole source $\vec{p}_1$ located inside the active layer of an OLED can be obtained by calculating the resulting electric field $\vec{E}_{p_2}$ inside the active layer by an imaginary dipole source $\vec{p}_2$ located far above the OLED in the direction of the desired emission angle.

In order to calculate $\vec{E}_{p_2}$, the electric field of the incident wave $\vec{E}_{p_2}^{inc}$ from the dipole $\vec{p}_2$ first needs to be found. If the distance *r* between the two dipoles $\vec{p}_1$ and $\vec{p}_2$ is sufficiently large and $\vec{p}_2$ is chosen to be a unit vector perpendicular to the wavevector of the incident wave $\vec{k}^{inc}$ (which does not restrict the generality), the incident wave can be considered as a plane wave and the electric field $\vec{E}_{p_2}^{inc}$ is given by

$$\vec{E}_{p_2}^{inc} = \frac{k^2}{4\pi\varepsilon_0 r} e^{ikr} e^{i\vec{k}^{inc}\cdot\vec{r}} \vec{p}_2 \quad (4)$$

where ε_0 is the permittivity in vacuum and $\vec{k}^{inc} = -k\hat{k}$ ($\hat{k}$ is a unit vector). Once $\vec{E}_{p_2}^{inc}$ is known, the electric field $\vec{E}_{p_2}$ inside the OLED can be calculated by solving the Helmholtz equation with appropriate boundary conditions:

$$\mu_r^{-1} \nabla \times \left(\nabla \times \vec{E}\right) - k_0^2 \varepsilon_r \vec{E} = 0 \quad (5)$$

where μ_r is the relative permeability, ε_r is the relative permittivity and k_0 is the wavevector in vacuum.

This step requires numerical computation using a rigorous method for each orthogonal polarisation state.

When the distance *r* is sufficiently large and $\vec{p}_2$ is chosen to be a unit vector, **Eq. 3** can be further expressed as

$$\lim_{r\to\infty}\left|\vec{E}_{p_1}\right|^2 = \lim_{r\to\infty}\sum_{v=S,P}\left|\vec{E}_{p_1}\cdot\vec{p}_2\right|^2 = \sum_{v=S,P}\left|\vec{E}_{p_2}\cdot\vec{p}_1\right|^2 \quad (6)$$

where *v = S,P* denotes s- and p-polarisation respectively. The overall emission intensity in the direction $\hat{k}$ contributed by incoherent dipoles located at position $\vec{r}_1$ in the active layer, and with random orientations of dipole vector $\vec{p}_1$, can be obtained by integrating the emission intensities over all orientations of $\vec{p}_1$.

$$I(\hat{k},\vec{r}_1) = \frac{1}{2}\sqrt{\frac{\varepsilon_0\varepsilon_2}{\mu_0}}\frac{1}{4\pi}\int_0^{2\pi}\int_0^{\pi}\left[\sum_{v=S,P}\left|\vec{E}_{p_2}\cdot\vec{p}_1\right|^2\right]\sin\theta\, d\theta d\varphi \quad (7)$$

where θ is the elevation angle, φ is the azimuthal angle, ε_2 is the relative permittivity at position $\vec{r}_2$ and μ_0 is the permeability in vacuum. If the dipoles are not isotropically oriented, the integration in Eq. 7 needs to be adjusted accordingly. Finally, as **Eq. 7** only consider dipoles located at position $\vec{r}_1$ inside the active layer, the calculation of the emission intensity from the entire OLED requires an integration over the whole recombination zone.

$$I(\hat{k}) = \iiint I(\hat{k},\vec{r}_1)\, d^3\vec{r}_1 \quad (8)$$

Using **Eq. 8**, the simulation of emission intensity at any single direction for any number of incoherent dipoles at any position in the OLED can be simplified into only two simple calculations on a unit cell of the periodic structure.

The unit cell of a test microstructured OLED is shown in **Fig. 1b**. The whole unit cell was constructed in a commercial modelling software COMSOL Multiphysics v4.4, which uses the FEM to solve **Eq. 5 to 8**. The top surface in **Fig. 1b** is defined as the input port, where the incident plane wave $\vec{E}_{p_2}^{inc}$ propagates into the device structure. The four surrounding surfaces are defined as periodic boundary conditions, which consider all the diffraction orders of the grating. In order to accurately simulate the wave propagation, the maximum mesh size of the geometry is defined as less than one eighth of the wavelength in each layer. The overall emission intensity is integrated over the entire active layer and a sweep of different combinations of elevation angles and azimuthal angles is simulated in order to obtain the overall emission intensity. The overall emission intensity in the free space hemisphere can be plotted in a projected disk, as shown in **Fig. 1c**. The *x*-ordinate on the projected disk is defined as $\cos\theta\cos\varphi$ and the *y*-ordinate is defined as $\cos\theta\sin\varphi$.

To accurately calculate the emission pattern, a sufficient density of angular coordinates is required. However, if the elevation and azimuthal angles are sampled on an equidistant grid, an unpractically large number of simulations can be necessary in order to capture the most directional features. To solve this problem, an adaptive sampling method was applied to locate the diffracted peaks more efficiently. In this sampling method, a relatively small number of equidistantly spaced angles were simulated initially, and then an algorithm (written in Matlab) determined the additional angles requiring simulation. The

algorithm adds more angles around the local peak intensities for the simulation to find all peaks, and was also designed to distinguish two peaks that partially overlap. The adaptive calculation runs in an iterative loop and convergence is reached when the peak values become almost constant. A comparison of the initial and final simulated angles using such an adaptive sampling method is shown in **Fig. 1d**. Each dot in the graph represents an angle for simulation and the graph showing the final simulated angles has much denser dots in specific regions. Using the adaptive sampling method, the relative intensity of the maximum peak to the background can be quantified.

3. Experimental methods

In order to verify the accuracy of the model, microstructured OLEDs were fabricated and tested. A 240 nm-thick nanoimprint lithography (NIL) resist was spin-coated on the glass substrate and then brought in contact with a UV-cured polymer stamp which previously replicated the photonic microstructure pattern from a silicon master grating. After being cured by high dose UV exposure, the pattern was imprinted into the NIL resist and the resist film formed a square array pillar grating with a pillar height of around 100 nm. Three different grating periods 305 nm, 335 nm and 365 nm were fabricated. Further details of the UV-NIL procedure can be found in Ref [34]. The indium tin oxide (ITO) was deposited onto the corrugated NIL resist by radio frequency (RF) magnetron sputtering in vacuum using an Edwards AUTO 360 system. The chamber was pumped down to a base pressure of 1.8×10^{-6} mbar prior to the process. Sputtering was carried out in argon atmosphere at a pressure of 1×10^{-4} mbar. A 13.56 MHz RF power supply was used to provide the RF excitation. Plasma was generated with power of 70W. The thickness of the ITO was

around 260 nm and the resistance was 30 to 40 Ω/sq. A scanning electron microscopy (SEM) image of the top surface of the deposited ITO layer is shown in **Fig. 2**. Poly(3,4-ethylenedioxythiophene):poly(styrenesulfonate) (PEDOT:PSS), poly(9-vinylcarbazole) (PVK) and 4,4'-Dicarbazolyl-1,1'-biphenyl : 2-(4-biphenyl)-5-(4-tert-butylphenyl)- 1,3,4-oxadiazole : tris(dibenzoylmethane)mono(4,7-diphenylphenanthroline)europium(III) (CBP:PBD: $Eu(DBM)_3Bphen$) were deposited by spin-coating. 1,3,5-Tris(N- phenylbenzimidazol-2-yl)benzene (TPBI), lithium fluoride (LiF) and aluminium (Al) were deposited by vacuum evaporation. The detailed procedure can be found in Ref [35]. The thickness of each layer was 40 nm for PEDOT:PSS, 35 nm for PVK, 90 nm for CBP:PBD:$Eu(DBM)_3Bphen$, 60 nm for TPBI, 0.7 nm for LiF and 100 nm for Al. It is worth noting that it is very likely that the 0.7 nm LiF layer is in a transition from island-like structure to homogeneous structure [36,37]. Since the average thickness is much less than the wavelength of light, we assume the LiF film is homogeneous in the eigenmode analysis. Such a thin layer of LiF has negligible influence on the effective index and so for 3D models the LiF layer is omitted from the structure.

Due to the spin-coating deposition, the microstructure features are eventually smoothed out in the organic layers. This is also considered in the calculation of the unit cell. The active layer of the microstructured OLED is CBP:PBD:$Eu(DBM)_3Bphen$ and the light emitted inside the active layer escapes into free space through the glass substrate. Since the thickness of the glass substrate is around 1 mm, which is much larger than the coherence length of the device, the unit cell does not include the whole glass substrate in the calculation but only calculates the emission intensity from the organic layers into the glass substrate. The emission intensity in free space can be obtained by calculating the change in solid angles and transmission at the interface of glass/air. The Eu complex in the active layer dominates the

electroluminescence spectra of the devices. It peaks at 612 nm with a full-width-half-maximum of several nanometres. Therefore the emission wavelength simulated in the model was chosen to be 612 nm. The refractive indices and extinction coefficients of each layer were measured by ellipsometry and used in the model.

The angle resolved emission from the microstructured OLEDs was experimentally collected by a fibre coupled Andor DV420-BV CCD spectrometer. The fibre collector moved in a plane perpendicular to the glass substrate from the normal direction to 70° with an interval of 2°. This corresponds to a measurement along the horizontal cutline through the centre of the projected disk (blue cutline in **Fig. 1c**).

4. Results and discussion

We first used the reciprocity theorem to investigate the emission intensity at a fixed azimuthal angle (φ = 0°) with varied elevation angles (θ = 0° - 90°). The adaptive sampling method was also applied. The simulation was calculated in both s- and p-polarisation, as shown in **Fig. 3**. I_0^s and I_0^p are the integration intensities over the active layer region in s- and p-polarisation for a case where the refractive indices of all layers are set to 1.52, the refractive index of the substrate at 612 nm. When the grating period is at 305 nm, a dominating peak is found at an angle of 19.72° superimposed on a broad spatial emission background in s-polarisation, while the emission in p-polarisation does not exhibit strong peaks. This indicates that this device structure efficiently out-couples transverse electric (TE) modes but not

transverse magnetic (TM) modes. To understand this result, an eigenmode analysis was carried out to obtain the electric field distribution of the waveguide modes. The calculated electric field distributions are shown in **Fig. 4**. These show that there is one TE and one TM mode supported by the structure. Most of the TE mode is located in the ITO layer, and thus the corrugated interfaces of NIL resist / ITO and ITO / PEDOT:PSS give efficient out-coupling of the TE mode. On the other hand, most of the energy in the TM mode is located close to the metal cathode, where the interface of the organic layer and the metal were almost flat. Therefore the out-coupling of the TM mode is relatively weak.

Fig. 5 shows the electric field distribution $\vec{E}_{p_2}$ in the unit cell corresponding to the elevation angle that gives the maximum emission intensity from the OLED, and another angle, off resonance. When $\theta = 11.5^{o}$, the electric field is scattered by the grating, but there is no significant light in-coupling into the device. On the contrary, when $\theta = 19.72^{o}$, the incident wave is efficiently in-coupled into the device and forms a propagating waveguide. This indicates that if the molecules emit into the TE waveguide mode, the light would be efficiently out-coupled by the grating at this angle.

The polar angle of the emission peak changes as a function of azimuthal angle, due to the change in the in-plane wavevectors. The emission pattern for the full hemisphere was calculated with the adaptive sampling method. Since the grating structure was symmetric, only one eighth of the projected disk needed to be directly calculated ($\theta = 0^{o}$ - 90^{o} and $\varphi = 0^{o}$ - 45^{o}). The results are shown in **Fig. 6**. When the grating period is 305 nm, four strong emission curves are superimposed on the spatial emission background. These four curves correspond to the light out-coupling at diffraction orders of (1, 0), (-1, 0), (0, 1) and (0, -1) of the square array grating [15]. For longer grating periods, the grating vector decreases

and thus the four Bragg scattered arcs move closer. When the grating period is 365 nm, another four curves, which have slightly weaker emission, appear in the projected disk, which correspond to the light out-coupling at diffraction orders of (1, 1), (1, -1), (-1, 1) and (-1, -1). The emission intensity in the projected disk not only gives the information of the out-coupled diffraction orders, but more importantly gives the relative intensities of the peaks to the spatial emission background.

The calculated results and the experimental results were compared along the blue cutline in **Fig. 1c** and the comparison results are shown in **Fig. 7**. Blue curves show the calculated results and black circles show the experimental results. The calculated position of the diffracted peaks matched well with the experimental results. The experimentally measured peaks are broader and less strong compared to the calculated results. This is due to the fact that the simulation only calculates one wavelength and the broadening in the emission spectrum contributes to a broadening in the angular distribution. Also, any imperfection in the grating and non-uniformity in film thickness will weaken the emission intensity and broaden peaks.

5. Conclusions

In this paper, we demonstrate a method to quantitatively analyse the spatial emission pattern of microstructured OLEDs. Using the reciprocity theorem, the calculation of the emission in each direction in the far field can be simplified into two simple calculations of an incident plane wave propagating into a single cell of the periodic structure. This makes the modelling highly parallelisable and saves a large

amount of computational resources compared to forward modelling methods. An adaptive sampling method was also used to efficiently capture sharp maxima in the emission in the projected disk and able to calculate reliably the positions of the emission peaks and their relative intensities. Microstructured OLED devices with three different grating periods were investigated as a test. The peaks in the projected disk were linked to the waveguide modes in devices. The calculated results were in good agreement with experimental results. This optical modelling method gives a useful quantitative calculation tool to investigate and control the spatial emission pattern of microstructured OLEDs.

Acknowledgement

S. Zhang, E.R. Martins, G.A. Turnbull and I.D.W. Samuel are grateful to the Scottish Universities Physics Alliance (SUPA) and the Engineering and Physical Sciences Research Council (EPSRC) for financial support.

References

1. J. M. Lupton, B. J. Matterson, I. D. W. Samuel, M. J. Jory and W. L. Barnes, Appl. Phys. Lett. 77 (2000) 3340-3342.

2. B. J. Matterson, J. M. Lupton, A. F. Safonov, M. G. Salt, W. L. Barnes and I. D. W. Samuel, Adv. Mater. 13 (2001) 123-127.

3. J. M. Ziebarth, A. K. Saafir, S. Fan and M. D. McGehee, Adv. Funct. Mater. 14 (2004) 451-456.

4. C. J. Yates, I. D. W. Samuel, P. L. Burn, S. Wedge and W. L. Barnes, Appl. Phys. Lett. 88 (2006) 161105.

5. A. M. Adawi, R. Kullock, J. L. Turner, C. Vasilev, D. G. Lidzey, A. Tahraoui, P. W. Fry, D. Gibson, E. Smith, C. Foden, M. Roberts, F. Qureshi and N. Athanassopoulou, Org. Electron. 7 (2006) 222-228.

6. W. H. Koo, S. M. Jeong, F. Araoka, K. Ishikawa, S. Nishimura, T. Toyooka and H. Takezoe, Nat. Photonics 4 (2010) 222-226.

7. W. H. Koo, W. Youn, P. F. Zhu, X. H. Li, N. Tansu and F. So, Adv. Funct. Mater. 22 (2012) 3454-3459.

8. T. Bocksrocker, F. Maier-Flaig, C. Eschenbaum and U. Lemmer, Opt. Express 20 (2012) 6170-6174.

9. J.-B. Kim, J.-H. Lee, C.-K. Moon, S.-Y. Kim and J.-J. Kim, Adv. Mater. 25 (2013) 3571-3577.

10. Y. H. Kim, J. Lee, W. M. Kim, C. Fuchs, S. Hofmann, H.-W. Chang, M. C. Gather, L. Müller-Meskamp and K. Leo, Adv. Funct. Mater. 24 (2014) 2553-2559.

11. K. B. Choi, S. J. Shin, T. H. Park, H. J. Lee, J. H. Hwang, J. H. Park, B. Y. Hwang, Y. W. Park and B.-K. Ju, Org. Electron. 15 (2014) 111-117.

12. S. Zhang, G. A. Turnbull and I. D. W. Samuel, Appl. Phys. Lett. 103 (2013) 213302.

13. S. Zhang, G. A. Turnbull and I. D. W. Samuel, Adv. Opt. Mater. 2 (2014) 343-347.

14. T. Schwab, C. Fuchs, R. Scholz, A. Zakhidov, K. Leo and M. C. Gather, Opt. Express 22 (2014) 7524-7537.

15. G. A. Turnbull, P. Andrew, W. L. Barnes and I. D. W. Samuel, Phys. Rev. B 67 (2003) 165107.

16. L. Tutt and J. E. Revelli, Opt. Lett. 33 (2008) 503-505.

17. J. Hauss, T. Bocksrocker, B. Riedel, U. Lemmer and M. Gerken, Opt. Express 19 (2011) A851-A858.

18. W. L. Barnes, Journal of Modern Optics 45 (1998) 661-699.

19. H. Benisty, R. Stanley and M. Mayer, J. Opt. Soc. Am. A. 15 (1998) 1192-1201.

20. Y. R. Do, Y. C. Kim, Y. W. Song, C. O. Cho, H. Jeon, Y. J. Lee, S. H. Kim and Y. H. Lee, Adv. Mater. 15 (2003) 1214-1218.

21. Y. J. Lee, S. H. Kim, J. Huh, G. H. Kim, Y. H. Lee, S. H. Cho, Y. C. Kim and Y. R. Do, Appl. Phys. Lett. 82 (2003) 3779-3781.

22. J. W. Kim, J. H. Jang, M. C. Oh, J. W. Shin, D. H. Cho, J. H. Moon and J. I. Lee, Opt. Express 22 (2014) 498-507.

23. J.-Y. Chen, J.-Y. Yeh, L.-W. Chen, Y.-G. Li and C.-C. Wang, Prog. Electromagn. Res. B 11 (2009) 15.

24. M. Slootsky and S. R. Forrest, Appl. Phys. Lett. 94 (2009) 163302.

25. T. Okamoto and K. Shinotsuka, Appl. Phys. Lett. 104 (2014) 093301.

26. X.-L. Zhang, J. Feng, J.-F. Song, X.-B. Li and H.-B. Sun, Opt. Lett. 36 (2011) 3915-3917.

27. H. A. Lorentz, *Versl. K. Akad. W Amsterdam, Collected Papers Vol III (Martinus Nijhoff, Hague, 1896)*, 4, 176, pp. 1-11.

28. R. J. Potton, Rep. Prog. Phys. 67 (2004) 717-754.

29. C. E. Reed, J. Giergiel, J. C. Hemminger and S. Ushioda, Phys. Rev. B 36 (1987) 4990-5000.

30. H. Rigneault, F. Lemarchand and A. Sentenac, J. Opt. Soc. Am. A. 17 (2000) 1048-1058.

31. A. L. Fehrembach, S. Enoch and A. Sentenac, Appl. Phys. Lett. 79 (2001) 4280-4282.

32. O. T. A. Janssen, A. J. H. Wachters and H. P. Urbach, Opt. Express 18 (2010) 24522-24535.

33. L. D. Landau and E. M. Lifchitz, *Electromagnetics of Continuous Media*. (Pergamon Press, Oxford, 1960).

34. G. Tsiminis, Y. Wang, A. L. Kanibolotsky, A. R. Inigo, P. J. Skabara, I. D. W. Samuel and G. A. Turnbull, Adv. Mater. 25 (2013) 2826-2830.

35. S. Zhang, G. A. Turnbull and I. D. W. Samuel, Org. Electron. 13 (2012) 3091-3096.

36. L. S. Hung, C. W. Tang and M. G. Mason, Appl. Phys. Lett. 70 (1997) 152-154.

37. F. R. Zhu, B. L. Low, K. R. Zhang and S. J. Chua, Appl. Phys. Lett. 79 (2001) 1205-1207.

Figures

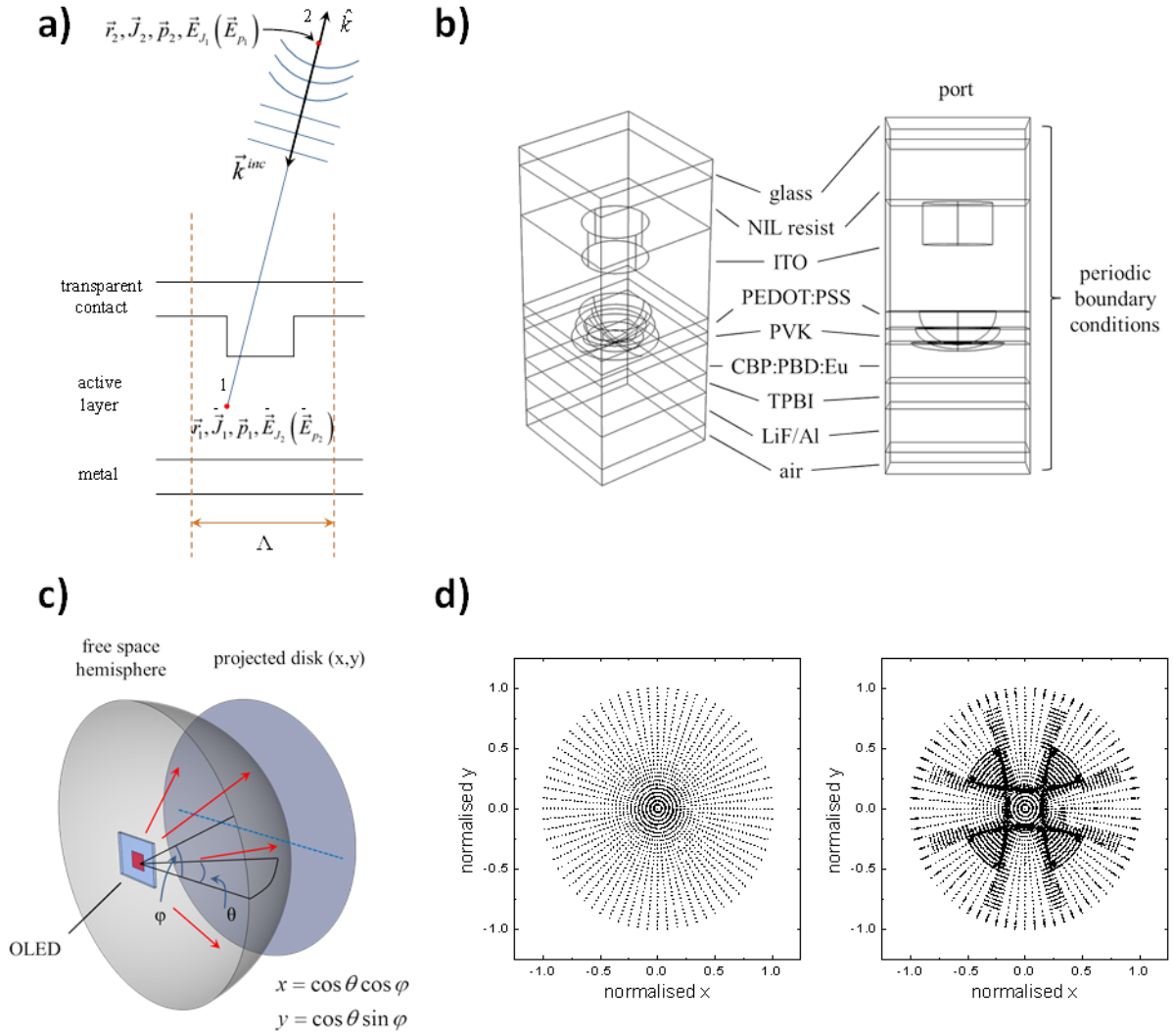

Fig. 1. a) Schematic diagram of a periodic cell of an OLED with two sources $\vec{J}_1$ and $\vec{J}_2$ at positions $\vec{r}_1$ and $\vec{r}_2$, and their corresponding electric fields $\vec{E}_{J_1}$ and $\vec{E}_{J_2}$. Point 1 is located in the active layer and point 2 is located in free space; b) the unit cell of a test microstructured OLED; c) diagram showing how the emission in the free space hemisphere can be plotted in a projected disk and d) comparison of the initial and final simulated angles using an adaptive sampling method (Each dot in represents an angle for simulation).

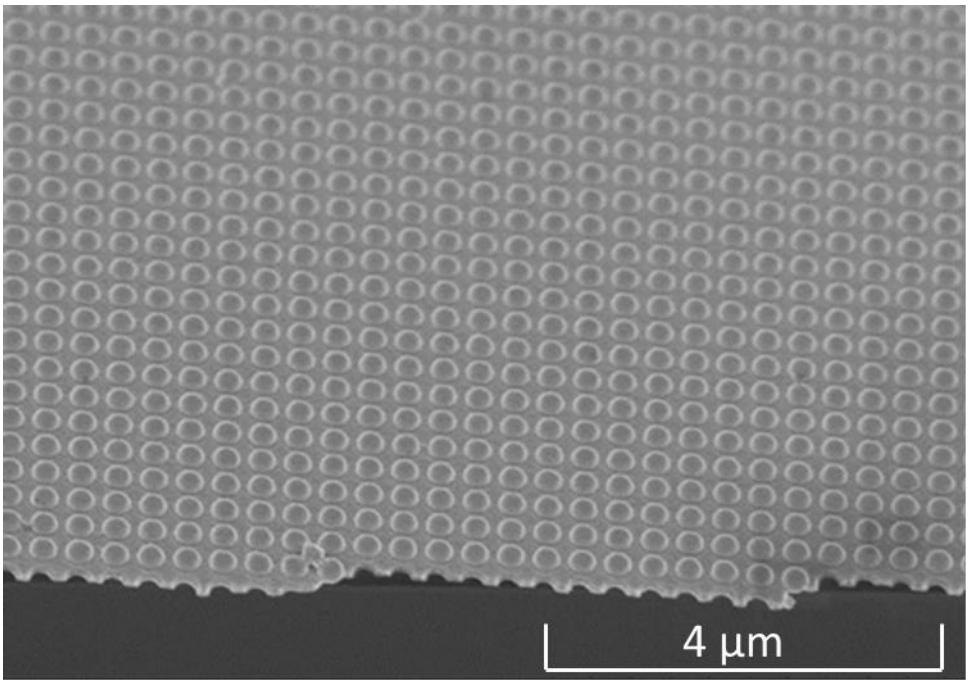

Fig. 2. Scanning electron microscopy (SEM) image of the top surface of the deposited ITO layer.

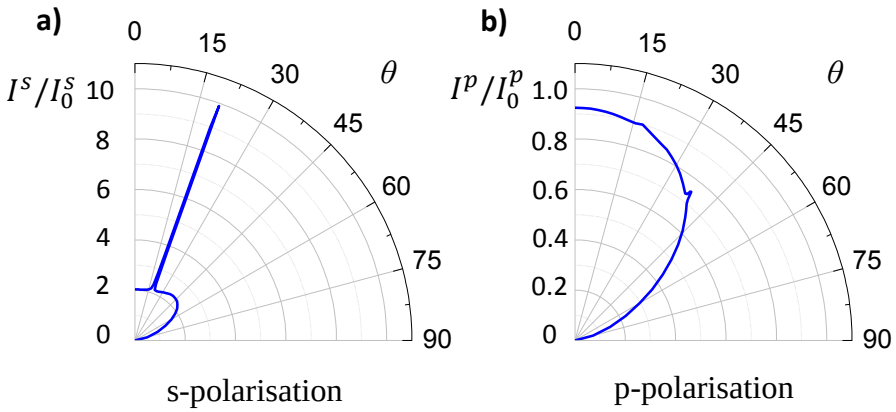

Fig. 3. Polar plots of calculated emission intensities in a) s- and b) p-polarisation as a function of elevation angle θ when the azimuthal angle φ = 0° and grating period Λ = 305 nm. Angles in the polar plots are shown in degrees. I_0^s and I_0^p are the integration intensities over the active layer region in s- and p-polarisation for a case where the refractive indices of all layers are set to 1.52, the refractive index of the substrate at 612 nm.

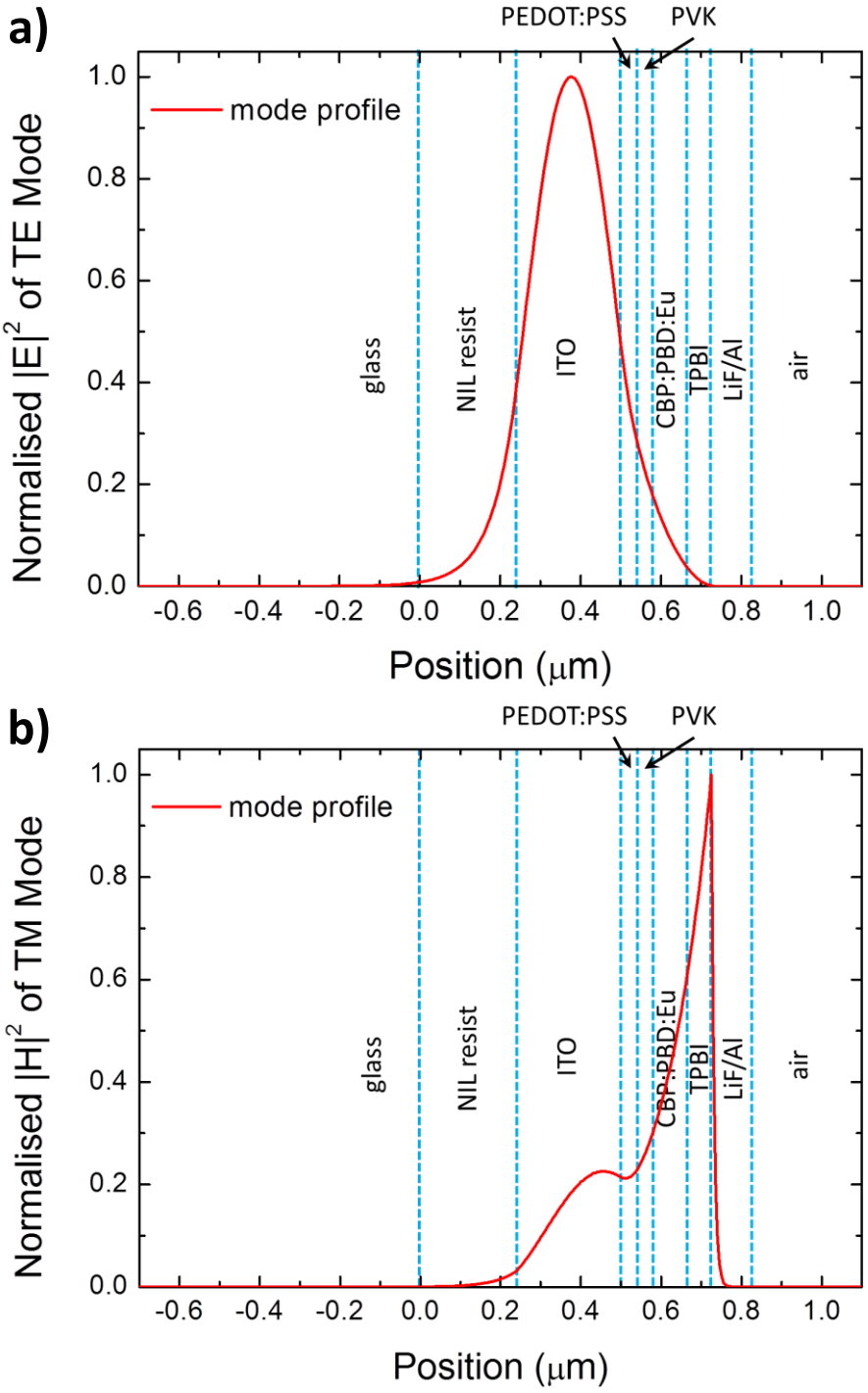

Fig. 4. The normalised intensity profiles of a) the TE mode in the s-polarisation and b) the TM mode in the p-polarisation in a planar OLED with deposited ITO.

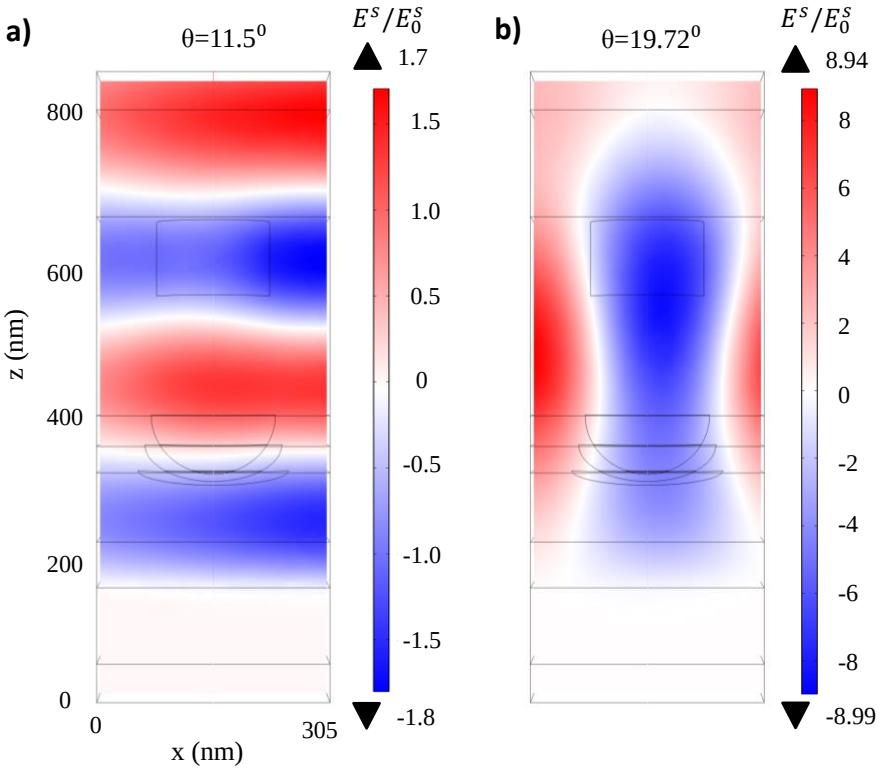

Fig. 5. Electric field distribution in the unit cell in s-polarisation when a) the elevation angle θ = 11.5° and b) the elevation angle θ = 19.72°.

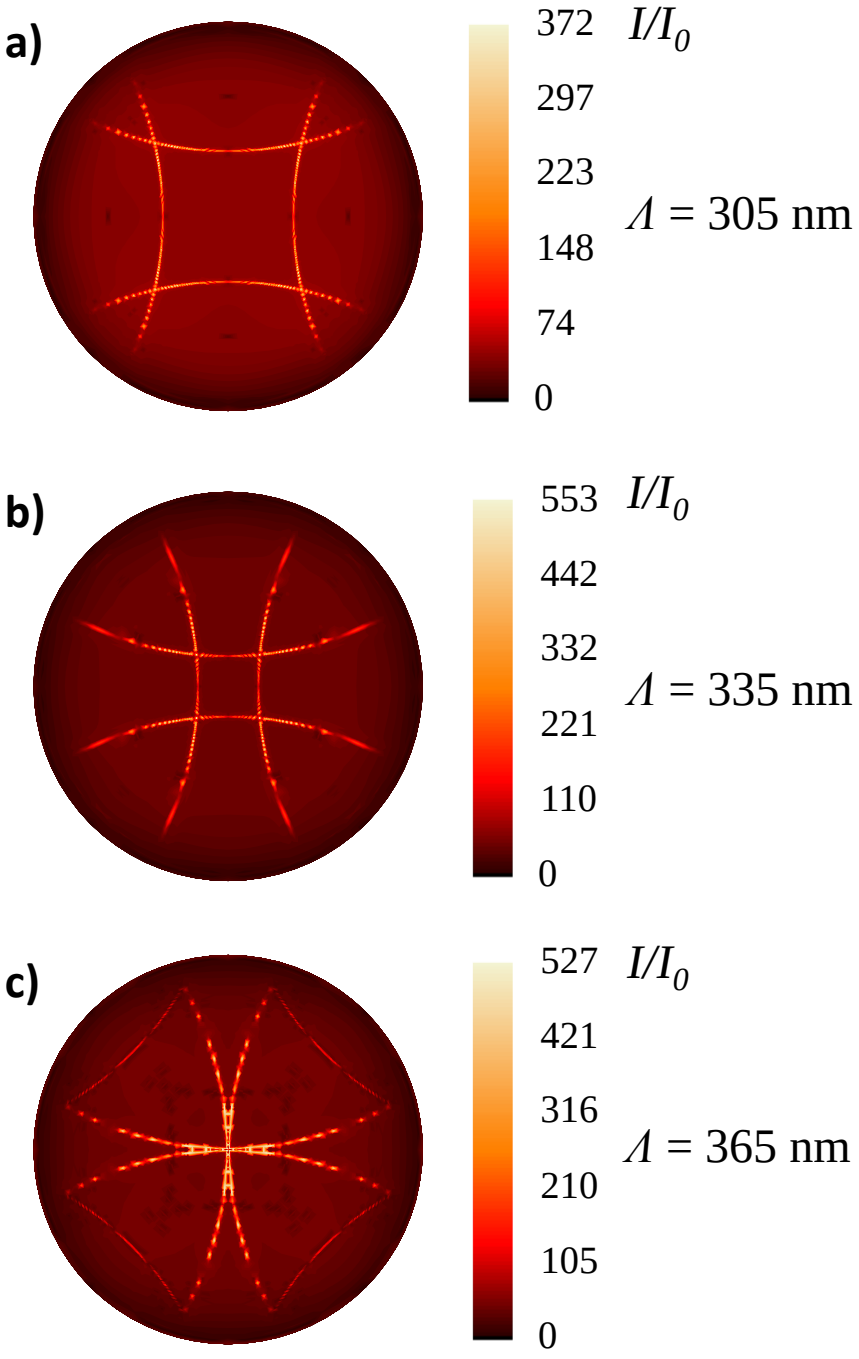

Fig. 6. The simulation results of spatial distribution of the emission intensities in the projected disk for microstructured OLEDs with grating period at a) 305 nm b) 335 nm and c) 365 nm using reciprocity theorem and adaptive sampling method. I_0 is the integration of the sum of the two polarisation components over the active layer region for a case where the refractive indices of all layers are set to be 1.52.

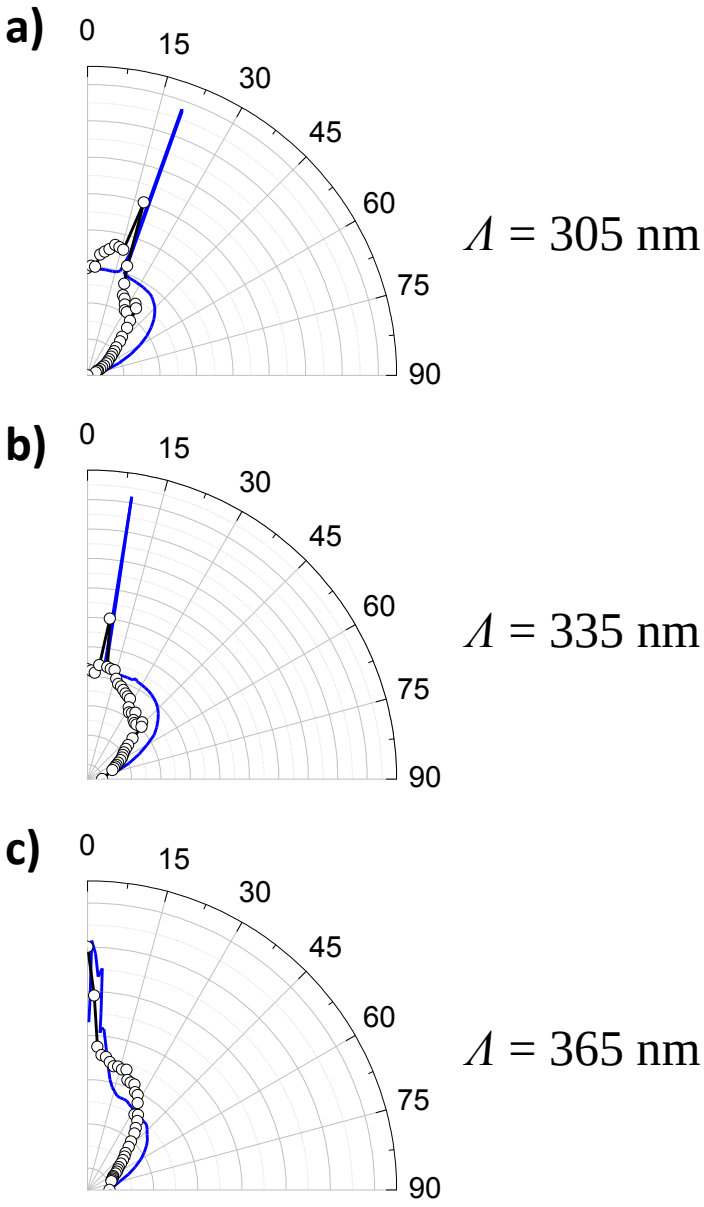

Fig. 7. Comparison of calculated spatial emission distribution with the experimental results along the blue cutline in **Fig. 1c** for microstructured OLED with grating period at a) 305 nm b) 335 nm and c) 365 nm. For each grating period, the calculated and experimental results are normalised at an angle of 0°. (blue curves are the calculated results and black circles are the experimental results)